J Mater Sci (2006) 41:4454–4465
DOI 10.1007/s10853-006-0153-1

Quantitative pressure and strain field analysis of helium precipitates in silicon

Norbert Hueging · Martina Luysberg · Helmut Trinkaus · Karsten Tillmann · Knut Urban

Received: 26 December 2005 / Accepted: 10 February 2006 / Published online: 7 July 2006

Abstract The structural properties of overpressurised helium precipitates formed by low dose ion implantation and subsequent annealing of silicon are investigated by quantitative transmission electron microscopy techniques. These precipitates, which show pronounced platelet geometry, are analysed with respect to their geometry, crystallographic orientation and their particular gas pressure values. The dependence of the measured platelet pressure versus the radius is discussed in terms of a Griffith crack. Experimental results on the shape and the crystallographic orientation of the platelets are discussed in the framework of anisotropic elastic properties and surface energies of silicon. The ability of the precipitates to punch-out dislocation loops is discussed in terms of associated threshold shear stress values and evaluated with regard to the defect size dependency.

Introduction

The understanding of the fundamental properties of helium in solids including its mobility and agglomeration has been an object of scientific interest for more than a decade as is impressively illustrated by a number of elaborate overview articles [1–3]. More recently, highly overpressurised helium precipitates formed in silicon upon implantation and subsequent annealing have become an object of particular interest for state-of-the-art microelectronic applications.

This interest results from the fact that the elastic strain relief of lattice parameter mismatched Ge_xSi_{1-x}/Si(001) thin layer systems can be substantially improved by helium ion implantation into the silicon substrates and subsequent annealing [4]. In the early stage of the thermal treatment, helium precipitates under high pressure appear [5], causing strong elastic strain fields in the substrate, which are supposed to induce the formation of dislocation loops. When these loops glide from the substrate region to the epilayer, certain segments are hold in the interface as misfit dislocations while the opposite segments are pulled to the surface. Under appropriate process conditions, threading dislocations formed between the interface and the surface annihilate each other almost completely [6]. By this means, a rather high density of threading dislocations in the epilayer can be avoided. Indeed, experimental analyses demonstrate a substantial improvement in the degree of relaxation as well as in the structural quality of helium implanted Ge_xSi_{1-x}/Si-heterostructures in comparison to conventional strategies of defect reduction [4, 7, 8].

For the emission of dislocation loops from the precipitates the most critical parameters are their geometry and particularly the ratio p/μ of the helium pressure to the silicon matrix shear modulus [9]. To test this basic aspect of strain relaxation it is therefore mandatory to determine the p/μ ratio of individual precipitates experimentally and to obtain detailed information on the evolution of both, the pressure and the geometry, in dependency of the annealing

N. Hueging · M. Luysberg · H. Trinkaus · K. Tillmann · K. Urban
Institute of Solid State Research, Research Centre Jülich, D-52425 Jülich, Germany

N. Hueging · M. Luysberg (✉) · K. Urban
Ernst Ruska-Centre for Microscopy and Spectroscopy with Electrons, Research Centre Jülich, D-52425 Jülich, Germany
e-mail: m.luysberg@fz-juelich.de

N. Hueging · M. Luysberg · H. Trinkaus · K. Tillmann · K. Urban
Center for Nanoelectronic Systems for Information Technology, Research Centre Jülich, D-52425 Jülich, Germany

conditions applied. In a recent paper [21] we focussed on a quantitative transmission electron microscopy (TEM) method to determine the pressure in dependence of the size of plate shaped precipitates. In the present analysis, these pressure values are examined in more detail. In particular, the stress fields surrounding the precipitates are evaluated in order to judge the ability of the precipitates to emit dislocation loops.

Since the temporal evolution of helium precipitates during the thermal treatment is rather complex and depends strongly on the chosen implantation and annealing parameters, a brief summary of the phenomena is appropriate in this introduction.

Upon implantation, high-energy He^+ ions mainly loose their kinetic energy by electronic excitation and Rutherford scattering inside of the crystal matrix. In case of a sufficiently high-energy transfer to the target atoms, point defects of Frenkel type, i.e. self-interstitial atoms and vacancies, are generated. The helium atoms come to rest in the silicon matrix where the corresponding depth profile can be calculated by numerical algorithms, e.g. by SRIM software (stopping and range of ions in matter software [10]). Focussing on room-temperature implantation, in the high-implantation dose regime ($\rho > 2 \times 10^{16}\,cm^{-2}$), spherical helium bubbles of a few nanometres in diameter are formed during the implantation procedure; this effect is not observed at implantation doses $\rho < 2 \times 10^{16}\,cm^{-2}$ [5, 11]. At intermediate doses of $1 \times 10^{16}\,cm^{-2} < \rho < 2 \times 10^{16}\,cm^{-2}$ small spherical bubbles are formed at annealing temperatures above 300 °C. In the low dose regime $5 \times 10^{15}\,cm^{-2} < \rho < 1 \times 10^{16}\,cm^{-2}$, helium atoms do not precipitate in spherical precipitates upon annealing but instead in planar defects mainly nucleating in parallel {100} planes. Below a threshold of $\rho < 5 \times 10^{15}\,cm^{-2}$ no extended defects are observed even after thermal treatment. The plate shaped precipitates decay at temperatures between 400 °C and 600 °C, i.e. a ring system of smaller spherical bubbles pinches off the platelet and the shape of the central precipitate transforms to spherical geometry simultaneously [12]. During annealing at even higher temperatures, helium dismantles from the bubbles and diffuses out, leaving depleted precipitates of a few nanometres in diameter behind. The uniform appearance of these bubbles does not allow for identification of the mechanisms controlling the precipitate morphology. In addition, helium implantation induced defects have been reported to be associated with dislocations. As an example, Oliviero et al. [13] observed cascades of dislocation loops lying on {111} glide planes after thermal treatment of helium implanted silicon at 800 °C which were supposed to be expelled by planar arrangements of spherical bubbles assumed to be large overpressurised platelets in an earlier evolution stage. In order to understand both, the evolution of the helium precipitation and the dislocation nucleation, it is hence essential to investigate the early stages of the annealing process.

In the present study we focus on the structural properties of helium precipitates in (001) oriented silicon substrates, which have been generated upon implantation and annealing in the low dose and low anneal temperature regime. The structural evolution in this early stage of precipitation is studied as a function of the annealing time. Geometrical characteristica are determined from transmission electron micrographs taken under kinematical conditions and the pressure values inside individual helium-filled platelets are measured by quantitative diffraction contrast imaging. Experimental data on the ratio of the pressure to silicon shear modulus p/μ of individual precipitates are discussed in terms of an overpressurised ''Griffith crack'' in mechanical and thermal equilibrium with the surrounding crystal matrix including the ability to produce dislocation loops.

Experimental procedure

A customary Si(001) substrate was implanted at room temperature using an Axcelis Medium Current Implanter 8250 choosing an He^+ ion energy of 40 keV at a dose of $\rho = 8 \times 10^{15}\,cm^{-2}$. The incident He^+ beam was directed along the crystallographic [$1\bar{1}0$] direction of the substrate, which ensures a laterally homogeneous distribution of implanted atoms at a position about 400 nm below the substrate surface. From the implanted substrate quadrangular pieces of 2 cm × 2 cm in size were thermally treated at $T = 400$ °C for times between 1 min and 70 min by rapid thermal annealing in an argon atmosphere. To simplify the further description, the samples will be labelled according to annealing temperature and time, e.g. Si400-10 will indicate an annealing temperature $T = 400$ °C at a duration of 10 min, in the following.

From these samples electron transparent cross sectional and plan view specimens were prepared by standard mechanical polishing procedures followed by Ar^+ ion milling at 4 keV under liquid-nitrogen conditions until perforation and, subsequently, at 2 keV to minimise the thickness of an amorphous surface layer induced by the ion milling process itself.

The geometry and the spatial arrangement of the cavities were analysed by conventional TEM of plan-view and cross-sectional samples using a magnification calibrated Philips CM20 instrument equipped with a field emission gun and operated under parallel illumination conditions at an acceleration voltage of 200 kV. Experimental images have been recorded on image plates with a discretisation of 3,760 × 3,000 picture elements using a instrumental

magnification of 98,833. To investigate the geometry and spatial distribution of the defects plan view specimen were imaged under kinematical conditions close to the [001] zone axis of the samples. For the quantitative determination of the pressure induced lattice displacements in the vicinity of the overpressurised precipitates, bright-field and dark-field micrographs as well as the corresponding selected area diffraction patterns were taken under dynamical **g** = (004) two-beam imaging conditions. These micrographs were analysed by an image processing routine as described in Section ''Impact of the pressure within precipitates on dislocation formation'' and used for extracting intensity line profiles along the [001] direction to be compared with numerically evaluated images.

Morphology and evolution of the precipitates

Geometry and spatial arrangement

Figure 1 shows a bright-field micrograph taken close the $[0\bar{1}1]$ zone axis orientation of a cross-sectional specimen from sample Si400-10. To elucidate the geometry of the preceding experimental treatment the crystallographic directions are indicated. The helium implantation occurred parallel to the $[\ 00\bar{1}]$ direction. A band of precipitates is visible below the free surface of the silicon substrate. Due to elastic distortions of the silicon matrix, the surrounding of the precipitates appears dark in contrast, which allows a direct identification of the vertical precipitate positions along the direction of implantation. In reverse, this dark contrast area gives evidence for considerably overpressurised precipitates. When analysing the complete set of samples investigated in this study, a commonly positioned and narrow band of precipitates is observed at a depth of 388 ± 23 nm below the surface of the substrate, independent of the annealing temperature and time chosen.

As illustrated by the plan-view micrographs taken from the same sample Si400-10 under kinematical conditions, cf Fig. 2, each element of the ensemble of precipitates is composed of a rather complex sub-structure consisting of one central plate-shaped precipitate surrounded by a ring system of smaller spherical bubbles of 2 to 5 nm in diameter. The central precipitates are characterised by diameters in the range of 40 to 120 nm and by a surface normal solely oriented along crystallographic $\langle 100 \rangle$ directions. They appear approximately circular in shape. A slight tendency towards faceting is observed when viewed with an electron beam roughly perpendicular to the (001) crack surface. The precipitates appear slit-like when viewed edge-on. In general, the mutual in-plane distance of these central precipitates clearly exceeds their average diameter. When measuring the shortest as well as the longest lateral axes and using an elliptic approximation a mean difference of 9.3% between both axes is found. Neglecting this minor difference, we may refer to the larger central precipitates being platelet or crack like in shape. By measuring a large number of micrographs an average platelet density of $\langle \rho \rangle = 11 \pm 2 \times 10^{-6}\ \mathrm{nm}^{-2}$ at an average equivalent radius of $\langle r_0 \rangle = 38 \pm 11$ nm is obtained for sample Si400-10.

Nearly all platelets in this sample nucleate with a surface normal parallel to the {100} planes of the silicon matrix. However, among these three crystallographically equivalent {100} planes, a preferential orientation of the platelets parallel to the substrate surface, i.e. to the (001) plane, is observed comprising 66% of all precipitates while the (010) and (100) orientations are found with an occurrence of only 19% and 15%, respectively. Because of this preferential alignment the most effective way to investigate the platelets edge-on, is to image cross-sectional samples.

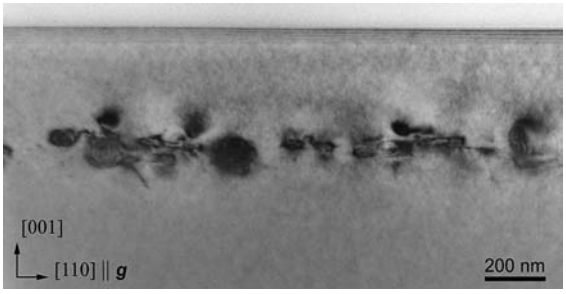

Fig. 1 Bright-field micrograph of sample Si400-10 taken close to the [110] zone axis of a cross-sectional specimen. A shallow band of precipitates is visible approximately 390 nm below the free surface of the silicon substrate

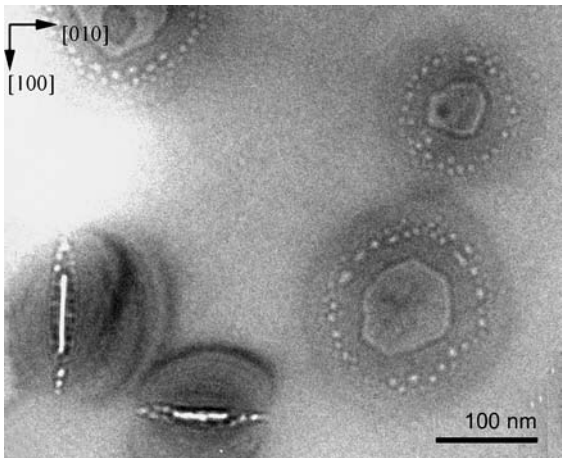

Fig. 2 Bright-field micrograph of sample Si400-10 taken under kinematical conditions at an underfocus excitation of the objective lens close to the [001] zone axis of a plan view specimen. The platelet precipitates, which slightly tend towards faceting parallel to various crystallographic directions, are oriented with a surface normal along the $\langle 100 \rangle$ directions and are surrounded by a ring system of smaller spherical bubbles

As illustrated by Fig. 3a, the platelets appear as bright slits according to the underfocused, bright-field two-beam imaging conditions using **g** = (004). Under these strongly dynamical imaging conditions, fringe systems surrounding the platelets are visible due to the deformation of the silicon matrix caused by the pressure inside the precipitates. The origin of these fringe systems, which allow for an accurate determination of the precipitate pressure, is similar to the classical Ashby-Brown diffraction contrast [14, 15] associated with lattice mismatched precipitates and will be explained in more detail in Section ''Impact of the pressure within precipitates on dislocation formation''. These fringes are, however, not observed in the very thin regions of the TEM specimens, where the platelets have been cut during sample preparation and only pressureless defects are left.

The micrograph shown in Fig. 3b represents a cross-sectional view of such a residual defect, which originally was an overpressurised platelet prior to the entire release of helium during the sample preparation. Its radius of $r_0 = 38$ nm coincides with the average radius $\langle r_0 \rangle$ noted before, so we may also take the thickness $2r_1 \leq 4$ nm as typical for the precipitates. Since there is no elastic deformation remaining in this region, a residual volume in absence of pressure in the precipitate can be calculated as $\langle V_{\mathrm{cra}} \rangle = \pi \langle r_0 \rangle^2 \, 2 \langle r_1 \rangle = 18.1 \times 10^3$ nm^3 and will be denoted as residual volume in the following. Now the residual volume provided by the ring system of smaller spherical bubbles will be assessed. To get an upper-bound estimate we consider a typical number of bubbles of $N_{\mathrm{bub}} \leq 30$ at radii $\langle r_{\mathrm{bub}} \rangle \leq 2$ nm as gained e.g. by the analysis of micrographs as displayed in Fig. 2. Using these values we obtain a typical volume of the ring system of $V_{\mathrm{bub}} = 4 \times \pi/3 \times N_{\mathrm{bub}} \langle r_{\mathrm{bub}} \rangle^3 \approx 500$ nm^3, which represents just a few percent of the total residual volume. In the following we may, hence, reasonably neglect the impact of the smaller bubble system.

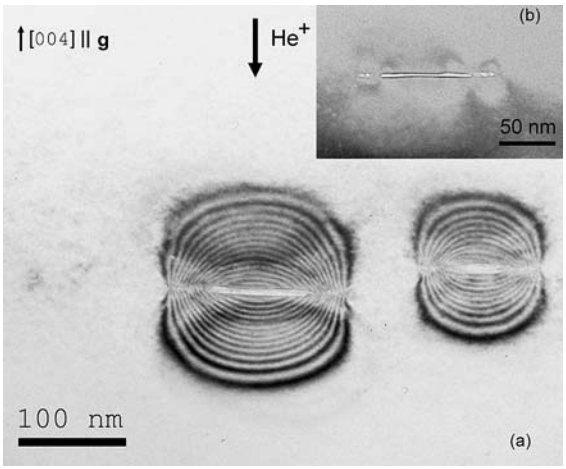

Fig. 3 (**a**) Bright-field micrograph taken close to the [1$\bar{1}$0] zone axis orientation of a cross-sectional sample and recorded under dynamical two-beam imaging conditions with **g** = (004). The overpressurised platelets are encircled by a system of contrast fringes. (**b**) These fringes are not observed in thinner regions of the TEM sample where the escape of helium leaves only a plate shaped void

Putting to use a few estimates we can assess the quantity of vacancies needed to form the volume defects. For these purposes we determine the defect volume in the samples. Quantitative measurements at more then 100 precipitates, e.g. in sample Si400-10, revealed an average radius of $\langle r_0 \rangle = 38$ nm and $\langle r_1 \rangle = 2$ nm as well as a platelet density of $\rho_{\mathrm{Plate}} = 11 \times 10^{-6}$ nm^{-2}. Using the penny-shaped approximation for the platelets we gain a typical defect density needed for this process of $\rho_{\mathrm{Va}} = 1 \times 10^{15}$ cm^{-2}. By stopping and range of ions in matter calculations (SRIM) [10] the Helium concentration and the vacancy concentration, which are plotted versus the depth in Fig. 4, are obtained. The vacancy concentration profile reveals, that a density of $\rho_{\mathrm{Va}} = 1 \times 10^{15}$ cm^{-2} may be provided even inside a rather small depth band of a few nanometres when assuming that the precipitates nucleate in the region of the highest defect density. Even if most of the point defects produced during implantation do recombine afterwards it is, hence, reasonable to assume that the platelet residual volume can be provided mainly by vacancy point defects. This will still be true facing the measurement uncertainty of $\langle r_1 \rangle = 2 \pm 1$ nm causing tremendous changes of the determined defect volume.

Discussion of platelet crystallography

In order to interpret the crystallographic orientation and the temporal evolution of the platelet geometry we start by considering the nucleation of small helium clusters, their growth and ripening and, finally, the decay of the precipitates upon thermal treatment. Concerning the first process, the nucleation of smaller clusters, we have no direct access by using TEM. The formation of clusters of helium atoms and vacancies $\mathrm{He}_m\mathrm{V}_n$ has been, however, discussed in several previous studies [11, 16, 17]. For the case of low availability of vacancies after recombination of most of them with self-interstitial atoms, the formation of helium interstitial clusters between lattice planes of the matrix has been proposed [9, 18]. If these clusters and/or helium atoms agglomerate they widen the surrounding crystal and finally will form a planar crack. At this point the description of the defects changes from an atomic to a mesoscopic scale. This concept is supported by the experimental finding of plate shaped central precipitates surrounded by a ring system of spherical bubbles and is in fair agreement with previous analyses demonstrating the existence of crack like precipitates in silicon [19]. Although these analyses demonstrated a minor number of

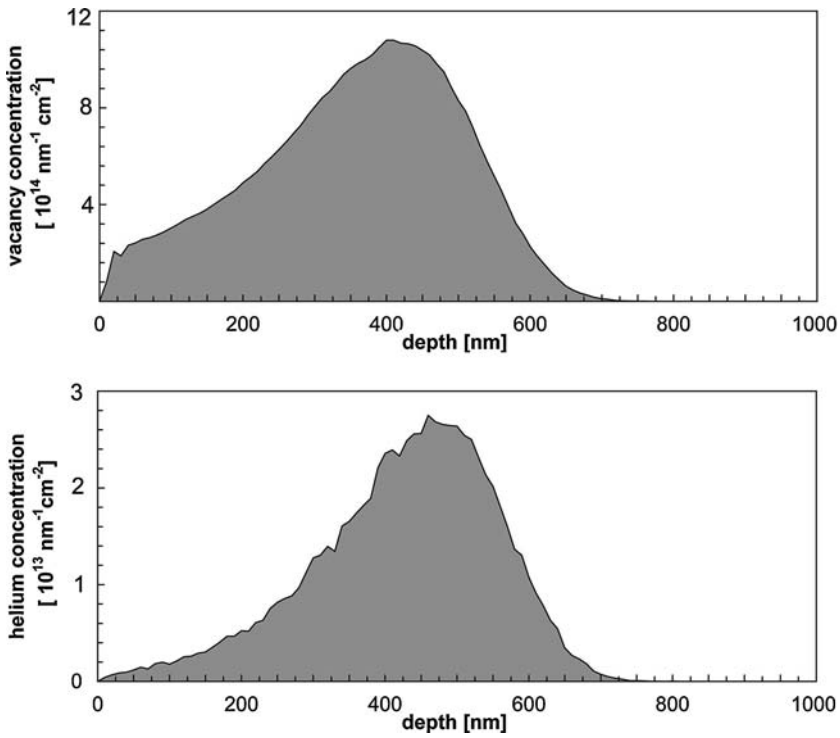

Fig. 4 Helium atom (**a**) and vacancy (**b**) concentration as gained by SRIM calculations assuming the implantation of 50,000 helium atoms to a Si(001) substrates at an ion energy of 40 keV. Density values refer to an implantation dose $\rho = 8 \times 10^{15}$ cm^{-2} as used during experiments in this study

platelets nucleated on {110} planes, the dominating habit planes observed were the {001} planes as observed in the present study.

Due to the anisotropy of the silicon lattice the agglomeration process will occur differently for various {*hkl*} planes. In a first approach the precipitation can be treated by using an energy approach in the isotropic approximation, which then can be extended to the anisotropic case. For this purpose, we first consider the free energy of a platelet with large axis r_0 and a total volume $V = V_0 + V_{el}$, where V_0 and V_{el} are the contributions due to the stress-free residual volume and the elastic volume resulting from the pressure induced displacement, respectively. This platelet is filled with N_g gas atoms. In the ''Griffith crack'' approximation the free energy F_{pl} is given by [9]:

$$F_{pl} = 2\pi r_0^2\gamma + \pi^2/6 \times Cr_0u^2 + F_{gas}(V) \quad \text{with} \quad C = 2\mu/(1-\nu) \tag{1}$$

Here, the first, second and third terms represent the contributions to the energy of the platelet surface (characterised by a specific surface free energy γ), of the elastic field associated with the elastic crack (with an opening displacement u, the shear modulus μ and Poisson's ratio ν), and of the gas atoms contained in the crack, respectively. Minimisation of F_{pl} with respect to u and r_0, i.e. $\partial F_{pl}/\partial u = 0$ and $\partial F_{pl}/\partial r_0 = 0$, using $p = -\partial F_{gas}/\partial V$, yields the pressure p and the displacement u for a crack in equilibrium

$$p = \frac{\pi\, Cu}{4\, r_0} = \sqrt{\frac{\pi\, C\, u}{2\, r_0}} \tag{2}$$

$$u = \sqrt{\frac{8\nu r_0}{\pi C}} \tag{3}$$

In the following discussion of the preferential platelet orientation, we focus on the parameter dependence of the free energy F_{pl} and ignore, for simplicity, numerical factors (of the order of 1) which are irrelevant for the arguments. Expressing r_0 in Eq. (1) and (2) by the elastic Volume V_{el}

$$V_{el} = (V - V_0) \sim r_0^2 u \sim \nu r_0^2/C, \tag{4}$$

we may write the parameter dependencies of Eq. (1) and (2) for F_{pl} and p, respectively, in the forms

$$F_{pl} \sim \left[\gamma^3 C_2 (V - V_0)^4\right]^{1/5} + F_{gas}(V), \tag{5}$$

$$p\left(V/N_g\right) \sim \left[\gamma^3 C_2\right]/(V - V_0)\big]^{1/5} \tag{6}$$

Equation (6) in conjunction with an equation of state, $p(V/N_g)$, defines a relation between the total volume V and the parameter $\alpha = (\gamma^3 C^2/V_a)^{1/5}$, where we have introduced

the atomic volume $V_a = 2 \times 10^{-2}\,\mathrm{nm}^3$ to obtain the dimension of a pressure for α. Using this in Eq. (5) to express V in $F_{gas}(V)$ by α, we find that the total free energy F_{pl} is a function of α and V_0 which increases monotonically with increasing α:

$$F_{pl} \sim \alpha. \tag{7}$$

In an anisotropic crystal such as silicon, the free energy of a gas filled platelet has the same form as Eq. (1), but now with appropriate anisotropic parameters γ and C (and correspondingly the combined quantity α) depending on the platelet orientation. The anisotropic specific surface (interface) free energy to be used, γ_{hkl}, is obviously that of the habit plane {hkl} of the platelet. For the elastic constant, we have to use an appropriate anisotropic extension of C, for instance on the basis of elastic constants for an uniaxial strain or an uniaxial stress in the direction normal to the habit plane {hkl} of the platelet. We favour the uniaxial stress approximation since the deviation of the elastic constant C in Eq. (1) for elastic isotropy from that for an uniaxial stress is only of second order in ν ($\approx$0.2 for silicon), as can be seen by expressing C by the elastic compliance $S_{11}/C = 2\ \mu\ (1-\nu) = 1/((1-\nu^2)S_{11})$. Accordingly, we introduce an anisotropic pressure parameter characterising the orientation dependence of the free energy and the pressure of the platelets

$$\alpha_{hkl} = \left(\frac{\gamma_{hkl}^3}{S_{hkl}^2 V_a}\right) \tag{8}$$

where S_{hkl} are the ''longitudinal'' elastic compliances along the $\langle hkl\rangle$-directions, obtained from the standard compliances [20] by the relation

$$S_{hkl} = S_{12} + \frac{1}{2}S_{44} + \frac{S_a(k^4 + k^4 + l^4)}{(h^2 + k^2 + l^2)^2} \tag{9}$$

with the anisotropic compliance

$$S_a = S_{11} - S_{12} - \frac{1}{2}S_{44} \tag{10}$$

Energetically, platelets should favour habit planes $\{hkl\}$ where γ_{hkl} is small as possible. In Table 2, values of the anisotropic parameters γ_{hkl}, S_{hkl} and α_{hkl} are listed for the main crystallographic planes and directions, respectively. The value of γ_{hkl} is minimum for {111} planes, whereas S_{hkl} is maximum for the elastically softest $\langle 100\rangle$ directions. In spite of the higher weight of γ_{hkl} (power of 3) in α_{hkl}, S_{hkl} (power of 2) dominates the α_{hkl} value. Accordingly, the {100} planes represent the energetically most favourable habit planes for gas-filled platelets which is in agreement with our observations. We emphasize that the same ranking list of α_{hkl} values would be obtained, even though less well separated, if instead of S_{hkl} the corresponding C_{hkl} were used for α_{hkl} evaluation.

There remains, however, the question why (001) platelets parallel to the sample surface are about four times more frequently observed than platelets oriented along the crystallographically equivalent (100) or (010) planes. It is obvious that this preference is due to the presence of the free (001) surface which has been neglected in the above considerations. In fact, the free surface reduces the stress field of a platelet and thereby introduces an attractive ''image'' interaction which results in a reduction of the free energy of the platelet. Since the stress field of the gas-filled platelets is more pronounced above and below than aside of them as shown by Figs. 2 and 3 (similar as for dislocation loops), this image interaction is stronger for platelets parallel than for those perpendicular to the surface—which explains, at least qualitatively, the observed preferential (001) habit plane of the platelets.

Structural decay of the platelets upon annealing

The helium platelets analysed in this study undergo a process of decay with increasing annealing time. The transformation of ideally plate shaped precipitates towards arrangements of central precipitates surrounded by a ring system of small bubbles has been previously reported [12]. This process of decay is illustrated by the micrographs displayed in Fig. 5a–c corresponding to annealing times of 1, 10 and 70 min respectively. The platelet-like precipitates and their ring systems of spherical bubbles are displayed at an approximate tilt of 20° from the edge-on orientation. The process of decay has already begun after the one-minute treatment. While the mean radius of the ring system does not significantly depend on the annealing time the central platelet undergoes a shape transformation by decreasing its radius r_0 coinciding with an increase in thickness as shown in Fig. 5d.

As a consequence, for increasing annealing durations the morphology of the platelets deviates more and more from the ideal shape of a Griffith crack, which would imply attenuated margins due to its elastic displacement field. This effect is already visible in sample Si400-10, cf Fig. 3. Thus, material transport processes resulting in shape and volume changes of the precipitates have to be considered. This consideration is also corroborated by the existence of slit-like notches observed in the thin regions of the TEM samples leading to the interpretation of residual volume. By this means the platelets leave an open gap whereas an ideal Griffith crack should collapse to zero volume. The intrinsic volume of the real inclusions most likely originates from the formation process of the precipitates and may turn out to

play an even more important role in the process of decay, providing empty voids even when helium diffuses out at high temperatures.

To discuss the precipitates shape transformation from platelets to spheres we may consider that helium filled precipitates are highly overpressurised and may have collected vacancies. At some point, the pressure inside the precipitate decreases because the helium supply ceases and helium diffuses out or further vacancies are collected. Therefore, the surfaces of a platelet come closer to each other and may collapse at some point resulting in a rim of bubbles surrounding the residual platelet as it is observed in this study. In addition, the largest shear stress values will be reached at the margin of the platelets since the whole pressure induced forces acting onto the cracks faces have to be compensated. By reorganisation of the precipitate surface, e.g. by surface diffusion, this extreme situation relaxes since at curved surfaces the strain energy is spread over a larger distance.

Impact of the pressure within precipitates on dislocation formation

Pressure within the precipitates

When experimental images are taken under well-defined dynamical imaging conditions a fringe system of bright and dark lobes is observed in the vicinity of plate shaped precipitates, as shown in Fig. 3a. In this micrograph the white and black contrast lobes meet close to the apex of the precipitates and show the maximum distance along a line through its centre parallel to the imaging vector $\mathbf{g} = (004)$. Since pioneering work of Ashby and Brown it is well known that the analysis of these characteristic contrast lobes represents a highly suitable method to determine the pressure value associated with spherical precipitates embedded in a crystal matrix [14, 15]. The basic idea of this technique is to image the displacement field in the vicinity of the precipitate resulting from the pressure induced force and to determine the pressure by adjusting calculated images up to the best possible conformity with the experimental observation.

This classical approach is, however, only applicable to spherical precipitates characterised by a rather simple elastic strain field and may therefore not be used for the observed platelet geometry. In the present study we employ a numerical extension to this classical approach to determine the pressure of the plate shaped precipitates, which is described in detail in reference [21]. The basic principle of the pressure measurement is the comparison of experimental diffraction contrast micrographs with image simulations. To solve the Howie–Whelan equations [22, 23] two-beam imaging conditions are assumed, which comply with the experimental situation chosen. For the analytical treatment of the elastic displacement field associated with the overpressurised precipitates, we approximate the platelet geometry by that of a circular crack in an elastic isotropic medium [24]. For a given precipitate radius, the distance of the contrast lobes from the centre of the platelet

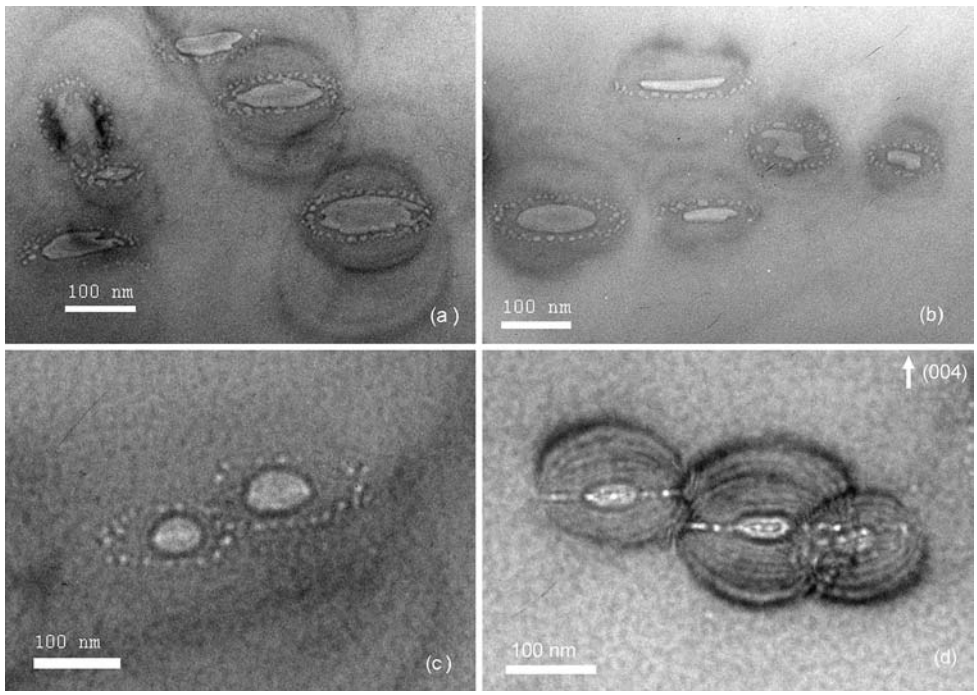

Fig. 5 Series of bright-field images taken under kinematical conditions showing platelets in the samples Si400-1 (**a**), Si400-10 (**b**) and Si400-70 (**c**) at an approximate 20° tilt out of their edge-on orientation and Si400-70 (**d**) in edge-on orientation illustrating the morphological evolution of helium platelets under thermal treatment. With increasing anneal time the central platelets undergo a structural transformation towards an ellipsoidal shape by decreasing the platelet radius and increasing their thickness

increases monotonically as the displacement fields and hence the pressure is increased. This functional dependency allows the unambiguous determination of the pressure, by comparing calculated and experimentally determined fringe extrema positions [21].

Following this procedure, the pressure p of about 20 platelets was measured from micrographs taken under two-beam dynamical imaging conditions. The results of these measurements are summarised in Fig. 6, where the pressure is plotted versus the precipitate radius together with two theoretical curves, which are described in sections ''Equilibrium model considerations'' and ''Ability of the precipitates to expel dislocation loops''. Pressure values are normalised to the isotropically averaged shear modulus $\mu = 68.14$ GPa of silicon. The data demonstrate a distinct increase of the pressure with decreasing platelet radii. Numerical values are in the range between $p/\mu = 0.07$ for $r_0 = 66$ nm up to $p/\mu = 0.22$ for $r_0 = 17$ nm. For values of $p/\mu > 0.17$ the helium is calculated to be solid even at room temperature [1]. Error bars along the p/μ axis represent the standard deviation of individual data points which have been averaged over experimental values obtained for single platelets imaged under five different excitation conditions. Individual values of the radii represent mean values of the platelet semi-axis lengths measured along two orthogonal directions from micrographs taken under kinematical conditions. The corresponding error bars, thus, reflect deviations from the assumed circular precipitate geometry.

Uncertainties in the experimental measurement of r_0 additionally lead to errors within the p/μ measurement procedure. Since fringe extrema positions in the images will also increase with increasing radii one risks to underestimate p/μ when overestimating r_0 and vice versa. This situation is illustrated in Fig. 6 for a single data point ($r_0 = 29$ nm, $p/\mu = 0.14$) by means of the slanted black line which describes the functional behaviour of the p/μ adjustment when changing the crack radius within the bounds of its inherent uncertainty while keeping all other parameters fixed.

Equilibrium model considerations

The most striking result of the pressure measurement is the distinct decrease of the pressure with increasing platelet radii. As discussed by Hartmann and Trinkaus [9] the condition describing a crack-shaped precipitate in equilibrium with its crystalline surrounding is given by (see Eq. (2)):

$$\left(\frac{p}{\mu}\right)_{\mathrm{eq}} = \sqrt{\frac{\mu\gamma}{(1-\nu)\mu}} \cdot \frac{1}{\sqrt{r_0}} \tag{11}$$

with γ denoting the specific interface free energy between the precipitate and matrix material. This theoretical equilibrium dependency is added to the experimental data points as a solid curve in Fig. 6 assuming material parameters according to Table 1 and an interface free energy of $\gamma = \gamma_{001} = 1.38$ Jm^{-2} according to Table 2. With these parameters, the equilibrium curve systematically underrates the experimental results by about 20% independent of the platelet radius. The measured increase of p/μ values with decreasing radii r_0 is, however, supported by functional behaviour of the model curve.

In general, the difference between the predicted curve and the experimental results may be due to numerical deviations in the chosen material parameters contained in Eq. (11), to systematic errors in the evaluation procedure, or it may be real in the sense that the crack-like precipitates are not in their stable equilibrium configuration.

As discussed by Tillmann et al. [21] in extenso, potential systematic errors in the analysis procedure due to the neglect of elastic anisotropy and non-linear elasticity effects or in the set of material parameters due to an increased specific surface free energy are partly compensating each other and the quantification of the net amount of all contributions is far beyond feasibility. However, according to the general tendency of the system to relax the pressure of the precipitates, Eq. (11) is expected to represent an upper estimate ruling out p/μ values above the solid curve in Fig. 6. Nevertheless the experimentally observed higher pressure values may, hence, be due to kinetic limitations of the precipitate growth resulting from the necessity of breaking atomic bonds at the apex of the platelets which may require overcritical p/μ values at annealing temperatures of only 400 °C. This limit applies particularly if the approximation of acute angles at Griffith cracks is abandoned and rounded rims of the platelet observed experimentally are taken into account. These rounded rims will result in moderated elastic stress values and, thus, retard a further lateral expansion of the platelets.

Ability of the precipitates to expel dislocation loops

Independent of the anneal conditions used, all samples investigated in this study show at least some platelets decorated with dislocations as is illustrated by Fig. 7a and b for sample Si400-1. The bright-field micrograph (a), which was taken under dynamical imaging conditions with $\mathbf{g} = (004)$, shows a discontinuity in the strain contrast induced fringe system visible as a shift on both sides of the dislocation line. This shift appears due to the strain field surrounding the dislocation core associated with a modification of the displacement field, which results in a phase shift in the dynamical description and consequently in a

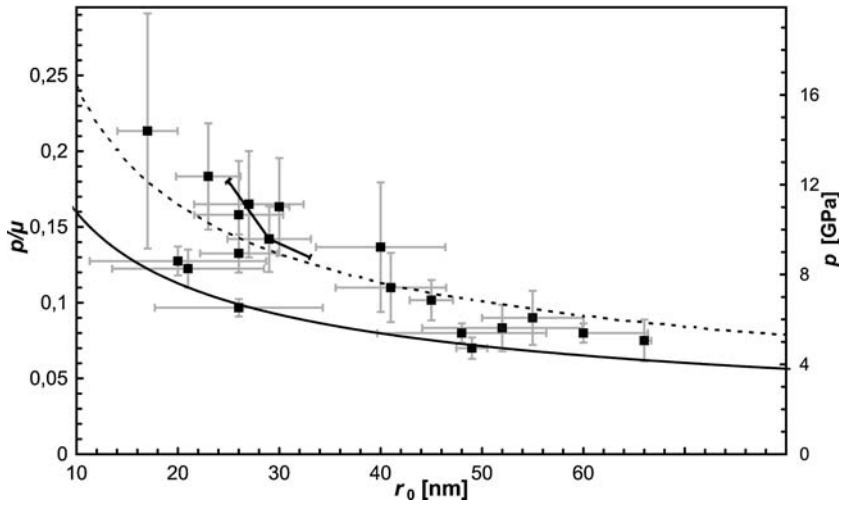

Fig. 6 Pressure to shear modulus ratio p/μ as a function of the radius r measured for individual platelets together with the equilibrium curve (solid line) according to Eq. (11) and the curve indicating the threshold pressure (dashed line) for dislocation loop nucleation. Error bars along the axis of ordinates represent the standard deviation associated with multiple measurements on the same platelet using different excitation conditions while error bars along the abscissa indicate measurement uncertainties in the determination of the precipitate radii

jump of the intensity across the dislocation line. Utilising weak beam imaging conditions, cf Fig. 7b, where the image contrast coincides with large displacement values, the pressure induced contrast fringes are only visible nearby the platelet. Consequently the dislocation extending into the silicon matrix appears as a white line.

The angle between the projection of the dislocation line and the (001) platelet amounts to about 35° when viewed along the [$1\bar{1}0$] zone axis of the sample, which implies a {111} habit plane of the dislocation loop and is typical for a prismatic dislocation loop [25]. The dislocation line ends at the rim of the platelet, i.e. within the region of the highest elastic stress values. This demonstrates that some of the platelets obviously have expelled dislocation loops.

Returning to the initial question whether and under which conditions the overpressurised platelets may contribute to the plastic relaxation of lattice mismatched Ge_xSi_{1-x}/Si(001) heterostructures the potential for the nucleation of mobile 60° dislocation loops close to the margins of the precipitates has to be discussed more in detail. If not untypical glide systems are activated at elevated temperatures, the nucleation and subsequent pinch-off of 60° dislocations in silicon usually takes place on {111} slip planes. This requires a minimum shear stress $\sigma_{\mathbf{b}} \approx \mu / (2() \approx 11$ GPa along the direction of the Burgers vector **b** [25].

From an elastomechanical point of view, the shear stress in the vicinity of the platelet is determined by the pressure and the geometry of the precipitate as well as by the material parameters of the silicon matrix. When considering a crack-shaped precipitate the pressure induced force acts perpendicular to the two circular surfaces bound together at their margins, where thus the largest shear stress values are expected. Hence, the shear stress distributions inside those {111} planes touching the outside border of the platelets determines the formation of dislocation loops. The geometry of this arrangement is illustrated in Fig. 8a. To simplify the further description within the depicted (111) plane we introduce a two-dimensional coordinate system with its origin $(\xi',\xi'') = (0, 0)$ characterising the cracks touching point, axes $\zeta' \parallel [\bar{1}\bar{1}2]$, and $\zeta'' \parallel [\bar{1}10]$. The two-dimensional greyscale image in Fig. 8b shows the distribution of the corresponding shear stress $\sigma_{\mathbf{b}}$ projected along the $\zeta = [0\bar{1}1]$ direction, which is assumed to be parallel to **b** inside the (111) slip plane of a 60° dislocation with a line direction $\zeta'' = [1\bar{1}0]$. By symmetry this stress distribution may, however, be transferred to other glide systems as well. The calculation is based upon the elastic strain field associated with a Griffith crack assuming a radius $r_0 = 20$ nm together with $p/\mu = 0.15$, i.e. structural parameters as experimentally measured for the smaller platelets according to Fig. 6. The upper half plane characterised by $\zeta \geq 0$ and $\sigma_{\mathbf{b}} \geq 0$ thus directly passes away from the crack while the lower half plane runs towards the centre of the crack.

The corresponding value of the shear stress $\sigma_{\mathbf{b}}$ projected on the Burgers vector direction ζ is shown in a line plot representation in Fig. 8c. The value of $\sigma_{\mathbf{b}}(\zeta)$ shows local maxima close to $\zeta = 0$, i.e. close to the position representing the boundary point between the (111) slip plane and the margin of the platelet. In both directions the absolute values decrease with increasing distance from the crack. Due to the different positions ''below'' and ''above'' the platelet ($\zeta \geq 0$ and $\zeta \leq 0$, respectively) the shear stress shows different absolute values for both directions. The functional behaviour of the curve demonstrates

slightly increased numerical values of $\sigma_{\mathbf{b}}$ for the upper half plane $\zeta \geq 0$ on the average, while peak values close to the crack are greatest at the lower half plane. Both branches exhibit shear stress values well above 8 GPa ($\zeta \geq 0$) and even 13 GPa ($\zeta \leq 0$) at distances given by the length of the Burgers vector $|\mathbf{b}| = a/\sqrt{2} \approx 0.4$ nm to the crack margin. Applying the criterion that the critical shear stress $\sigma_{\mathbf{b},\mathrm{crit}} = \mu/(2\pi) \approx 11$ GPa is necessary to expel dislocation loops from the cracks [25], loop formation and gliding inside the lower half planes may be regarded as more favourable. In contrast to this, due to moderate peak stress values a dislocation movement along the $\zeta > 0$ branch may be regarded as less favourable, which is experimentally corroborated by the defect arrangement shown in Fig. 7.

Utilising the $\sigma_{\mathbf{b},\mathrm{crit}}$ criterion we determine the radius dependency of the critical p_{crit}/μ value for $\zeta \leq 0$. Since the analytical description of the shear stress projection along ζ? is quite complicated this calculation is done numerically by instating increasing pressure values in a step size of $p/\mu = 0.001$ until the $\sigma_{\mathbf{b}}$ value exceeds the threshold value $\mu/(2\pi)$. The resulting data points are added to Fig. 6 as a dashed line. Assuming a power law dependence, the fit of the threshold curve yields to $p_{\mathrm{crit}}\mathrm{P}r^{-0.54}$ indicating that loop nucleation preferentially occurs at larger platelets. On the other hand, especially for smaller radii, some of the experimental pressure values are overcritical. Thus the pressure values should be sufficient to pinch-off dislocation loops, which was indeed occasionally observed, cf Figure 9. Therefore, we conclude that helium filled platelets act as dislocation sources. This is of particular importance when focusing on lattice mismatched heterostructures, e.g. Ge_xSi_{1-x}/Si(001), where image forces from the epilayer and the free surface will additionally contribute to pull out loops from the overpressurised platelets, as observed in recent in-situ TEM analyses showing the emission of dislocations loops from helium filled platelets [26].

Table 1 Silicon material parameters and properties: lattice parameter a together with the elastic constants c_{ij} and compliances S_{mn} according to [20]

Parameter	Silicon data value
A [nm]	0.54307
C_{11} [GPa]	165.77
C_{12} [GPa]	63.93
C_{44} [GPa]	79.62
S_{11} [10^{-12} Pa^{-1}]	7.68
S_{12} [10^{-12} Pa^{-1}]	2.14
S_{44} [10^{-12} Pa^{-1}]	12.6
μ [GPa]	68.14
ν	0.2175

Data on the shear modulus μ, and the Poisson's ratio ν represent isotropically averaged quantities calculated as $\mu = (c_{11}-c_{12})/5 + 3\,c_{44}/5$ and $\nu = (c_{11} + 4\,c_{12}-2\,c_{44})/(4\,c_{11} + 6\,c_{12} + 2\,c_{44})$ respectively [25]

Table 2 Surface energies of silicon for several major surfaces {*hkl*} according to Eaglesham et al. [27]

Parameter	Silicon data value
γ_{100} [Jm^{-2}]	1.36
γ_{110} [Jm^{-2}]	1.43
γ_{111} [Jm^{-2}]	1.23
γ_{113} [Jm^{-2}]	1.38
S_{100} [10^{-12} Pa^{-1}]	7.68
S_{110} [10^{-12} Pa^{-1}]	5.92
S_{111} [10^{-12} Pa^{-1}]	5.33
S_{113} [10^{-12} Pa^{-1}]	6.57
α_{100} [10^{-12} Pa]	18.4
α_{110} [10^{-12} GPa]	21.1
α_{111} [10^{-12} GPa]	20.1
α_{113} [10^{-12} GPa]	19.8

Longitudinal compliances S_{ll} for uniaxial stress in (*hkl*)-direction according to Eq. (8) and the corresponding parameter $\alpha(hkl)$ characterising the anisotropy of the total free energy F_{tot} for the {100} planes

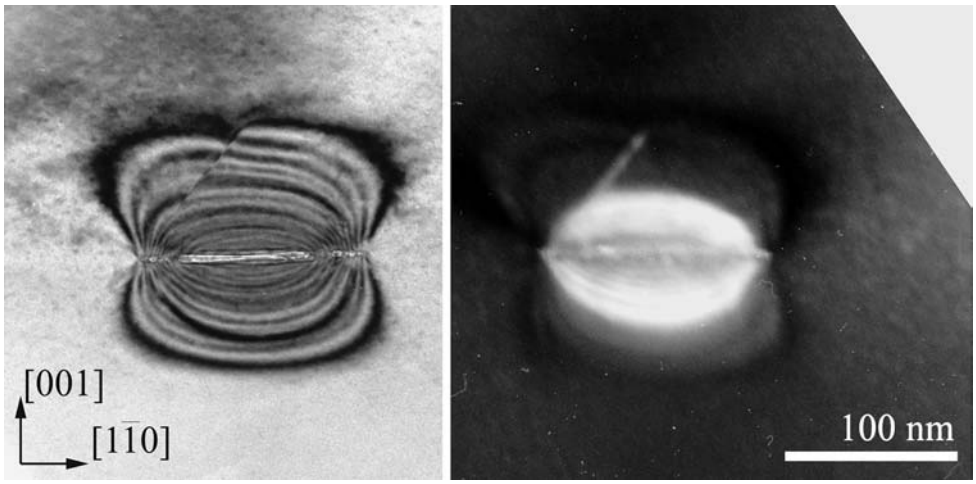

Fig. 7 (a) Bright-field micrograph taken close to the [1$\bar{1}$0] zone axis orientation of a cross-sectional sample recorded under dynamical two-beam imaging conditions with **g** = (004). The pinched-off 60° dislocation loop originating at the very margin of the platelet gives rise to a shift of the system of contrast fringes and gets more clearly visible in the corresponding micrograph taken under 4 · **g**/**g** weak beam imaging conditions (b).

Conclusions

The mechanisms of the nucleation and structural decay of helium filled precipitates in implanted and subsequently annealed silicon have been analysed by transmission electron microscopy. Helium ion implantation was carried out under room temperature conditions at an ion energy of 40 keV and a dose of 8×10^{15} cm^{-2}. When thermally treated at 400 °C for time intervals between 1 min and 70 min overpressurised helium filled platelets of some ten nanometres in radius and each surrounded by a ring system of smaller bubbles appear at a well-defined depth sector 388 ± 23 nm below the free surface of the substrate.

Due to the elastic anisotropy of silicon these platelets are exclusively oriented with a surface normal parallel to the crystallographic ⟨100⟩ directions with a preferential orientation along the (001) planes parallel to the free surface of the silicon substrate. Upon thermal treatment these platelets undergo a geometrical transformation towards spherical bubbles with increasing annealing time. This behaviour may be understood by surface diffusion driven by a tendency to minimise the total energy of the precipitate.

The pressure of the plate shaped precipitates was measured using quantitative electron diffraction contrast imaging. Independent of the anneal time chosen, the experimental results yield $0.07 \leq p/\mu \leq 0.22$ for platelet radii in the range $66\ \text{nm} \geq r \geq 17\ \text{nm}$. The observed functional behaviour p/μ indicates that the platelets are in, or at least close to, thermodynamical equilibrium.

The radius dependency of the threshold pressure criterion $\sigma_{\mathbf{b}} > \mu/2\pi$ was evaluated confirming that several precipitates, preferentially those with smaller radii, have the ability to emit dislocation. Numerical stress values indicate an intrinsic instability of the platelets to relax by plastic deformation through the formation of dislocation loops. In particular dislocations nucleated in this way may contribute to the relief of elastic strains in lattice parameter mismatched Ge_xSi_{1-x}/Si(001) thin layer structures.

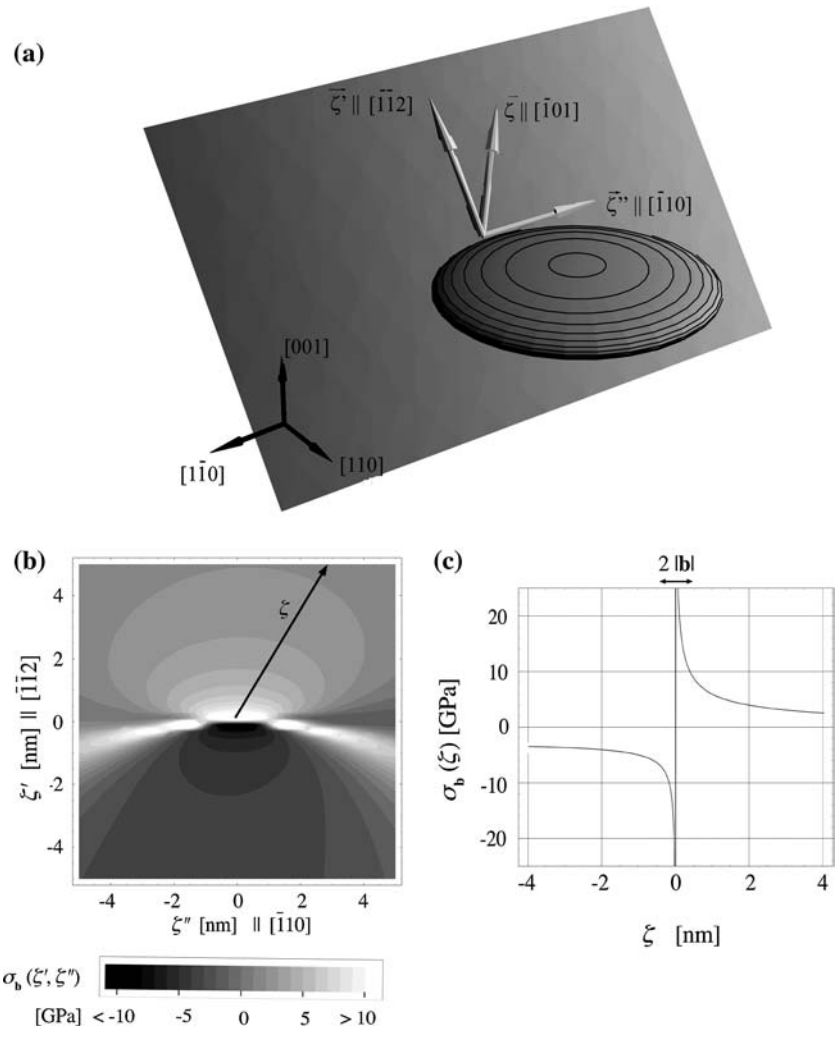

Fig. 8 (**a**) Geometrical illustration of a circular crack with a (001) surface normal and a {111} plane contacting the crack's margin. (**b**) Contour representation of the elastic shear stress distribution $\sigma_{\mathbf{b}}$ projected along the [$\bar{1}$01] direction of the Burgers vector **b**, which runs along the ζ direction inside the {111} slip plane together with (**c**) a line profile along the ζ direction touching the crack at $\zeta = 0$

Acknowledgements The authors cordially thank Bernd Holländer and Siegfried Mantl for the fruitful cooperation during realisation of the implantation experiments, for guidance of the SRIM calculations as well as for helpful discussions.

References

1. Trinkaus H (1983) Rad Effects 78:189
2. Donnelly SE (1985) Rad Effects 90:1
3. van Veen A (1991) In: Donnelly SE and Evans JH (eds) Fundamental aspects of inert gases in solids, Plenum Press, New York, p 41
4. Holländer B, St. Lenk, Mantl S, Trinkaus H, Kirch D, Luysberg M, Herzog H-J, Hackbarth T, Fichtner PFP (2001) Nucl Instr Meth Phys Res B 175–177:357
5. Fichtner PFP, Kaschny JR, Yankov RA, Mücklich A, Kreißig U, Skorupa W (1996) Appl Phys Lett 61:2656
6. Trinkaus H, Holländer B, St. Rongen, Mantl S, Herzog HJ, Kuchenbecker J, Hackbarth T. (2000) Appl Phys Lett 76:3552
7. Herve AJ, Bruel M (2000) Int J High Speed Electronics Syst 10:131
8. Luysberg M, Kirch D, Trinkaus H, Holländer B, St. Lenk, Mantl S, H.-Herzog J, Hackbarth T, Fichtner PFP (2002) J Appl Phys 92:4290
9. Hartmann M, Trinkaus H (2002) Phys Rev Lett 88:055505
10. Biersack JP, Haggmark L (1980) Nucl Instr Meth 174:257
11. Cerofolini GF, Corni F, Frabboni S, Nobili C, Ottaviani G, Tonini R (2000) Mater Sci Eng Reports 27:1
12. Fichtner PFP, Kaschny JR, Behar M, Yankov RA, Mücklich A, Skorupa W (1999) Nucl Inst Meth 148:329
13. Oliviero E, Beafort MF, Barbot JF (2001) J Appl Phys 89:5332
14. Ashby MF, Brown LM (1963) Phil Mag 8:1649
15. Ashby MF, Brown LM (1963) Phil Mag 8:1083
16. Raineri V, Saggio M (1997) Appl Phys Lett 71:1673
17. Brusa RS, Karwasz GP, Tiengo N, Zecca A (2000) Phys Rev B61:10154
18. Chen J, Jung P, Trinkaus H (2000) Phys Rev B61:12923
19. Fichtner PFP, Kaschny JR, Kling A, Trinkaus H, Yankov RA, Mücklich A, Skorupa W, Zawislak FC, Amaral L, da Silva MF, Soares JC (1998) Nucl Inst and Meth B 136–138:460
20. Hellwege K-H (eds) (1982) Landolt-Börnstein: numerical data and functional relationships in science and technology. New Series, Springer-Verlag, Berlin, p 17
21. Tillmann K, Hueging N, Trinkaus H, Luysberg M, Urban K (2004) Microsc Microanal 10:199
22. Howie A, Whelan MJ (1961) Proc R Soc A163:217
23. Howie A, Whelan MJ (1962) Proc R Soc A267:217
24. Griffith A (1921) Trans R Soc A221:163
25. Hirth JP, Lothe J (1968) Theory of dislocations. McGraw-Hill, New York
26. Hueging N, Luysberg M, Urban K, Buca D, Mantl S (2005) Appl Phys Lett 86:042112
27. Eaglesham DJ, White AE, Feldman LC, Moriya N, Jacobson DC (1993) Rev Lett 70:1643